Effects of Al addition and cryogenic cyclic treatment on impact toughness of phase-transformable Ti-based bulk metallic glass composites

Tingyi Yan [a b], Long Zhang [a c], R. Lakshmi Narayan [d], Jingyu Pang [a b], Yi Wu [a b], Huameng Fu [a c], Hong Li [a c], Upadrasta Ramamurty [e f], Haifeng Zhang [a c]

Abstract

Developing bulk metallic glass composites (BMGCs) with high toughness is vital for their practical application. However, the influence of different microstructures on the impact toughness of BMGCs is still unclear. The effects of Al addition and cryogenic cyclic treatment (CCT) on the Charpy impact toughness, a_K, at 298 and 77 K of a series of phase-transformable BMGCs are investigated in this work. It is found that deformation-induced martensitic transformation (DIMT) of the β-Ti dendrites is the dominant toughening mechanism in the phase-transformable BMGCs at 298 K, but at 77 K, the toughness of BMGCs is primarily determined by the intrinsic toughness of the glass matrix. The addition of Al can moderately tune the β-Ti phase stability, which then affects the amount of DIMT and impact toughness of the BMGCs at 298 K. However, at 77 K, Al addition causes a monotonic decrease in the toughness of the BMGCs due to the embrittlement of the glass matrix. It is found that CCT can effectively rejuvenate the phase-transformable BMGCs, which results in an enhanced impact toughness at 298 K. However, the toughness at 77 K monotonously decreases with increasing the number of CCT cycles, suggesting that the rejuvenation of the glass matrix affects the toughness at both 298 and 77 K of BMGCs, but in dramatically different ways. These findings reveal the influence of microstructures and CCT on the impact toughness of BMGCs and provide insights that could be useful for designing tougher BMGs and BMGCs.

Keywords

Bulk metallic glass composites; Charpy impact toughness; Deformation-induced martensitic transformation; Metastability; Thermal cycling rejuvenation

1. Introduction

Bulk metallic glasses (BMGs), which lack long-range atomic order, have superior mechanical properties, including high strength, high hardness, and large elasticity, which make them promising structural materials [1]. However, at room temperature or lower temperatures, the plastic strains in BMGs are highly localized in thin shear bands [2], [3], [4]. Shear bands are associated with local softening and dilatation, which causes strain localization, which in turn, manifests as a lack of tensile ductility and relatively low fracture toughness of BMGs [5], [6], [7], [8], [9]. To alleviate these drawbacks, bulk metallic glass composites (BMGCs) with a microstructure of in-situ formed crystals embedded in the BMG matrix have been developed [10], [11], [12], [13]. Ductile crystals in BMGCs homogenize plasticity by promoting the formation of multiple shear bands at glass-crystal interfaces and the effective arrest of shear bands, which dramatically improves the ductility and toughness [14], [15], [16], [17], [18]. Among these BMGCs, the Zr/Ti-based BMGCs containing β-Zr/Ti crystals have attracted extensive research interest due to the high glass-forming ability of the Zr/Ti-based glass matrix and the ability to control the microstructures with ease, including dendritic sizes, phase (meta)stability, and volume fraction of β-Zr/Ti crystals [14,15,[19], [20], [21]]. However, it has been revealed that the impact toughness, a_K, of BMGCs drastically decreases with decreasing temperatures [22,23], similar to that of monolithic BMGs, which is a deterrent in the context of their utility in low-temperature applications [24,25].

It has been shown that if the β-Ti dendrites are metastable phases, undergoing deformation-induced martensitic transformations (DIMT) to α′-Ti [26] or α″-Ti [27], [28], [29], [30], the BMGCs display large tensile plasticity concomitant superior work-hardening capacity, instead of work-softening and necking generally displayed by the BMGCs containing stable β-Zr/Ti crystals [28,29,[31], [32], [33]]. Also, it has been recently confirmed that phase-transformable BMGCs have higher a_K at low temperatures than BMGCs with stable β-Ti crystals, which is attributed to the fact that DIMT of β-Ti crystals absorbs impact energy over a wide temperature range [34]. Meanwhile, the BMGCs with the optimized dendritic size and volume fraction of phase-transformable β-Ti dendrites exhibit high a_K at both 298 and 77 K [34]. In another investigation, it was observed that the phase stability of metastable β-Ti crystals can be mildly tuned by Al addition [28], which significantly alters the strength and tensile ductility of BMGCs. However, how the mildly-tuned phase stability of β-Ti crystals affects a_K of BMGCs remains unknown.

Moreover, it has been widely reported that the ductility and toughness of BMGs and BMGCs are closely related to the energy states of the glassy phases [35], [36], [37], [38], [39], [40], [41]. Recently, many methods, including cryogenic cyclic treatment (CCT) [38,42], shot-peening [43], ion irradiation [44,45], and twin-roll casting by squeezing the supercooled liquids during producing strips [36], have been employed to considerably rejuvenate BMGs and BMGCs. Some investigations [41,42,[46], [47], [48]] show that the rejuvenation by CCT is sensitive to the composition, initial energy state, and thermal history in terms of improving fracture toughness. For instance, Li et al. [42] found that the K_{IC} of Zr-based BMGs increased by 50% after 70 times of CCT, whereas different non-monotonic changes were found in Pd-based and Zr-based BMGs by Ketkaew et al. [46]. For BMGCs, Rajpoot et al. [38] found that 30 times

CCT increases the compressive plasticity of Zr-based BMGCs, but it is ineffective in enhancing fracture toughness. It is noteworthy that these studies were carried out at room temperature and at low strain rate loading conditions. Therefore, it is not clear how CCT affects the deformation behavior and a_K of phase-transformable BMGCs under impact loading at 298 and 77 K.

In this work, the effects of Al addition and CCT on microstructures, deformation behaviors, and impact toughness at 298 and 77 K of a series of Ti-based $(Ti_{0.523}Zr_{0.346}Cu_{0.047}Be_{0.084})_{100-x}Al_x$ (at.%, labeled as Al*x*) BMGCs with phase-transformable β-Ti crystals have been systematically investigated. Both Al addition and CCT can significantly affect the impact toughness of the phase-transformable BMGCs. Based on the experimental results, the relationships between microstructures and impact toughness as well as the underlying fundamental deformation mechanisms are carefully revealed. Moreover, the different dominant mechanisms on impact toughness of phase-transformable BMGCs at 298 and 77 K are discussed in detail.

2. Materials and experiments

2.1. Material preparation

Alloys with nominal compositions of $(Ti_{0.523}Zr_{0.346}Cu_{0.047}Be_{0.084})_{100-x}Al_x$ (at.%, labeled as Al*x*, x = 0, 4, or 6) were produced by arc melting using high-purity Ti, Zr, Cu, Be, and Al metals (purities over 99.8 wt%) under a Ti-gettered high-purity argon atmosphere. The ingots were re-melted four times combined with magnetic agitation to ensure chemical homogeneity. The ingots were arc-remelted and poured into a copper mold to produce the large-sized BMGC plates with a dimension of 6 mm (thickness) × 12 mm (width) × 60 mm (length). Some of the Al0 samples were subjected to CCT between 298 and 77 K 10 or 30 times (referred to as Al0–10C and Al0–30C, respectively). For this, they were immersed in liquid nitrogen for 10 min, and then heated to room temperature and held for 10 min.

2.2. Microstructure characterization

Slices were transversely cut from the as-cast plates for characterization by means of X-ray diffraction (XRD, Philips PW 1050, Cu-Kα), scanning electron microscopy (SEM, Tescan Mira 3) combined with energy-dispersive X-ray spectroscopy (EDS) and electron back-scattered diffraction (EBSD). The volume fractions and sizes of phases were measured using the computer software Image J (https://imagej.nih.gov/ij). Differential scanning calorimetry (DSC, Netzsch 204F1) at a heating rate of 20 K min^{-1} was performed on all alloys to evaluate the glass transition temperatures (T_g), crystallization temperatures (T_x), and relaxation enthalpy (ΔH_{rel}). Thin slices were further ground and ion-milled using a Gatan 695 device for conducting transmission electron microscopy (TEM, JEM-2100F) investigations.

2.3. Charpy impact testing

According to the ASTM E23–2018 for Charpy impact toughness testing [49], the plates were cut into specimens with a dimension of 5 mm × 10 mm × 55 mm, a U-shape notch with a depth of 2 mm and a notch radius of 1 mm were processed in the middle of each specimen. The Charpy impact tests were performed on the Charpy impact instrument (ZBC2452-D) with a maximum hammer speed of 5.3 m s^{-1}. The temperature of the tested samples was controlled at 298 and 77 K. At least three samples for each BMGC were tested at each temperature. The fractured specimens were selectively characterized by means of SEM, EBSD, and TEM.

3. Results

3.1. Microstructures of the as-cast Alx BMGCs

The microstructures of as-cast Al*x* alloy plates are shown in Fig. 1. As can be seen from the XRD patterns in Fig. 1(a), sharp diffraction peaks from the body-centered cubic (BCC) phase superimposed on the broad hump are detected in all alloys, indicating the co-existence of β-Ti and amorphous phase. In addition, some small diffraction peaks, which correspond to α″-Ti are also observed in all three alloys. The SEM micrographs of Al*x* in Fig. 1(b–d) show the β-Ti dendritic phases are uniformly distributed in the glass matrix, and the volume fraction (~74%) of the dendrites are very similar. However, the average sizes of the secondary dendritic arms decrease gradually with Al addition, from 7.2 ± 1.9 μm in Al0 to 5.8 ± 1.8 μm in Al4 and to 3.9 ± 1.1 μm in Al6. The distribution of all constituents in the dendrites and matrix of the as-cast Al4 and Al6 BMGCs, as determined by the EDS compositional maps, is shown in Fig. S1 in the Supplementary Material. With the increase of Al, the contents of Ti and Zr in β-Ti decrease, but the content of Cu first increases and then decreases. The quantitatively-obtained compositions of β-Ti and the glass matrix in Al*x* BMGCs are also determined by the SEM-attached EDS, which are listed in Table 1. The enrichment of Cu and Al in β-Ti and the depletion of Zr will lead to the enhancement of the phase stability of β-Ti, which leads to the increase of the precipitation temperature of isothermal ω-Ti during the DSC heating [28,50]. As shown in Fig. S2, with increasing Al addition, the β → ω transition temperature increases from ~520 K for Al0 to ~700 K for Al4, but then decreases to ~650 K for Al6. Given that Al4 has the highest β → ω transition temperature, its β-Ti phase stability is highest compared to the other two alloys [28].

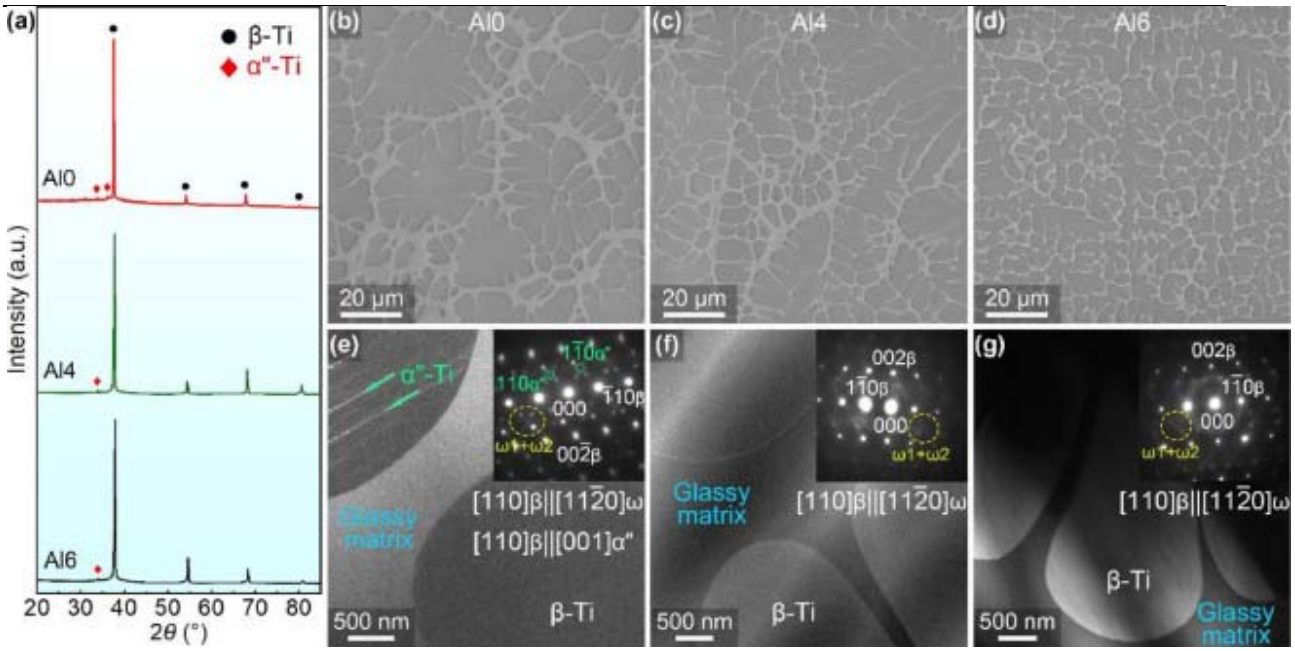

1. Download: Download high-res image (647KB)
2. Download: Download full-size image

Fig. 1. (a) XRD patterns, (b–d) SEM micrographs, and (e–g) TEM micrographs with insets of SAED patterns of the as-cast Al0, Al4, and Al6 BMGCs, respectively.

Table 1. The compositions and abbreviated names of the investigated BMGCs. The measured volume fraction, V_β, the average size of secondary β-Ti dendritic arms, S_d, and the EDS-determined compositions of both phases are also listed.

BMGCs	Compositions (at.%)	V_β (%)	S_d (μm)	Elemental content * (at.%)				
				Phases	Ti (±1.8)	Zr (±1.4)	Cu (±0.5)	Al (±0.3)
Al0	$Ti_{52.3}Zr_{34.6}Cu_{4.7}Be_{8.4}$	74.0 ± 1.8	7.2 ± 1.9	β-Ti	61.9	35.9	2.2	0
				Glass	42.6	43.5	13.9	0
Al4	$Ti_{50.2}Zr_{33.2}Cu_{4.5}Al_4Be_{8.1}$	73.3 ± 1.6	5.8 ± 1.8	β-Ti	59.9	33.6	2.3	4.2
				Glass	37.8	45.8	13.6	2.8
Al6	$Ti_{49.2}Zr_{32.5}Cu_{4.4}Al_6Be_{7.9}$	74.8 ± 2.2	3.9 ± 1.1	β-Ti	59.8	32.4	1.6	6.2
				Glass	36.4	45.3	14.3	4.0
Al0–10C	$Ti_{52.3}Zr_{34.6}Cu_{4.7}Be_{8.4}$	73.1 ± 2.2	7.1 ± 2.1	β-Ti	62.5	35.0	2.5	0
				Glass	42.4	43.5	14.1	0
Al0–30C	$Ti_{52.3}Zr_{34.6}Cu_{4.7}Be_{8.4}$	73.6 ± 2.4	6.9 ± 1.8	β-Ti	61.6	36.4	2.0	0
				Glass	43.1	42.5	14.4	0

* Beryllium cannot be detected by EDS, which has been revealed to be almost fully dissolved in the glass matrix [53].

Fig. 1(e–g) shows the TEM images of the as-cast Al*x* BMGCs. β-Ti phases are embedded in a featureless glass matrix for all Al*x* BMGCs. A few laths within the β-Ti dendrites, which were identified as α″-Ti by the selected-area electron diffraction (SAED) pattern in the inset of Fig. 1(e), were observed in Al0. The same was not observed in the dendrites of Al4 and Al6. In addition, athermal ω-Ti is also detected in SAED patterns in the zone axis of $[110]_\beta$ of all the Al*x* BMGCs (see insets), which is also an indicator of the relative phase stability of β-Ti [28,51,52]. Note that the ω-Ti diffraction spots are prominent and clearer in Al0 compared to that in Al6, whereas that of Al4 are the weakest. This suggests that the phase stability of β-Ti firstly increases and then decreases again with Al addition.

The EBSD results of the as-cast Al*x* BMGC microstructures are displayed in Fig. 2. From the phase maps in Fig. 2(a–c), it can be seen that β-Ti dendrites are homogeneously distributed in the glass matrix, while a small amount of α″-Ti (colored in red) can be detected in some of the β-Ti dendrites, which is precipitated at the interface between β-Ti and the glass matrix (Fig. 2(a)) [54]. The percentage of α″-Ti in the dendrites decreases with Al addition, i.e. it is 1.4% in Al0 but is hardly detected in Al4 and Al6 (Fig. 2(b, c)). This confirms our previous observations from TEM images in Fig. 1. The corresponding inverse pole figure (IPF) color maps of the Al*x* BMGCs are shown in Fig. 2(d–f). Different colors indicate different crystallographic orientations of dendritic phases. Although the volume fraction of β-Ti dendrites is similar in all three Al*x* BMGCs, the size of β-Ti

dendrites (regions with the same color) increases, but the size of secondary dendritic arms decreases with Al addition. The distribution of dendrite orientation in BMGCs deviates significantly from the random distribution and shows a certain texture. Generally, larger dendrites cause a more uneven local microstructure that will lead to higher texture intensity in BMGCs. The texture intensity, measured from the inverse pole figures, is 2.52 in Al0 but is considerably higher in Al4 (~4.73) and Al6 (~9.75), as shown in Fig. S3.

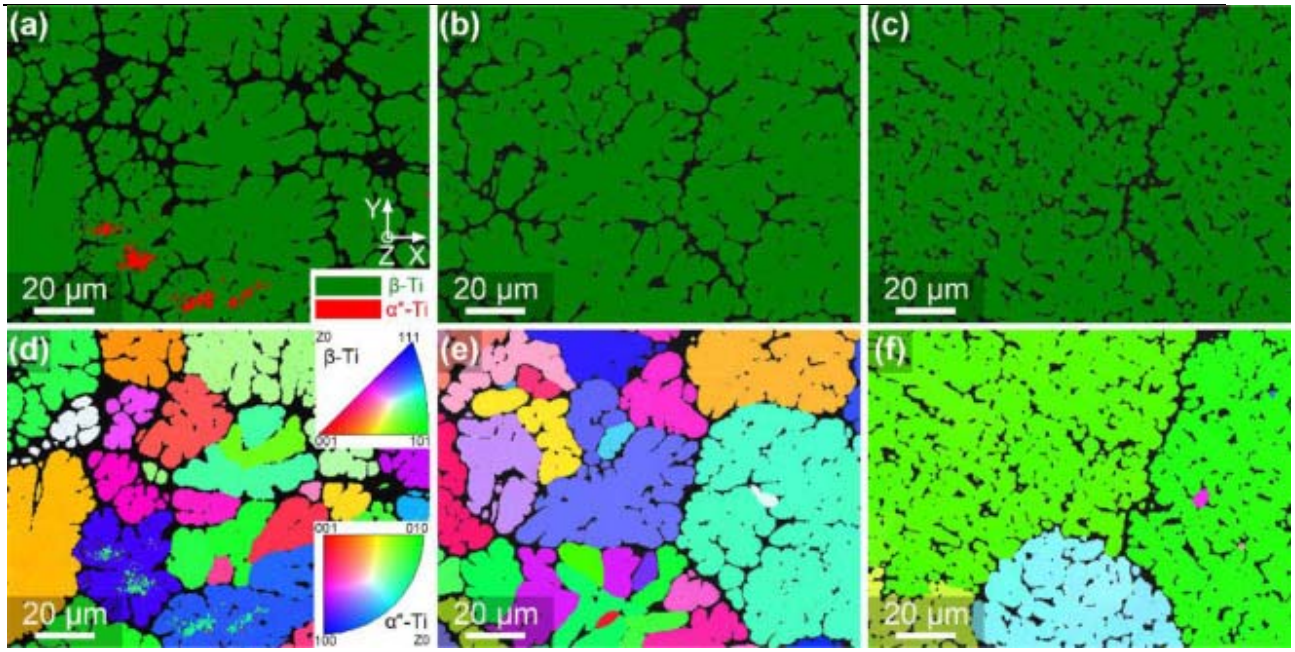

1. Download: Download high-res image (1MB)
2. Download: Download full-size image

Fig. 2. (a–c) Phase maps of the as-cast Al0, Al4, and Al6 BMGCs, respectively. (d–f) IPF color maps of the as-cast Al0, Al4, and Al6 alloys, respectively.

3.2. Impact toughness and fractured microstructures of Alx BMGCs

Fig. 3 displays the measured Charpy impact toughness, a_K, and the impact energy, A_K, of the Al*x* BMGCs tested at 298 and 77 K. The inset of Fig. 3 shows one typical image of the large-sized Charpy impact specimens used in this study. The measured a_K and A_K of the Al*x* BMGCs are also summarized in Table 2. At 298 K, a_K of Al0 is 24.8 ± 0.8 J cm^{-2}, but it slightly decreases to 22.8 ± 1.0 J cm^{-2} in Al4, and then again increases to 24.0 ± 0.8 J cm^{-2} for Al6. However, at 77 K, a_K of the Al*x* BMGCs exhibits a contrasting trend. While that of Al0 is 10.8 ± 0.8 J cm^{-2}, those of Al4 and Al6 are 8.5 ± 0.8 and 8.0 ± 0.5 J cm^{-2}, respectively. Overall, a_K is highest for Al0 at both 298 and 77 K. Alternately, a_K of Al4 and Al6 are lowest at 298 K and 77 K, respectively.

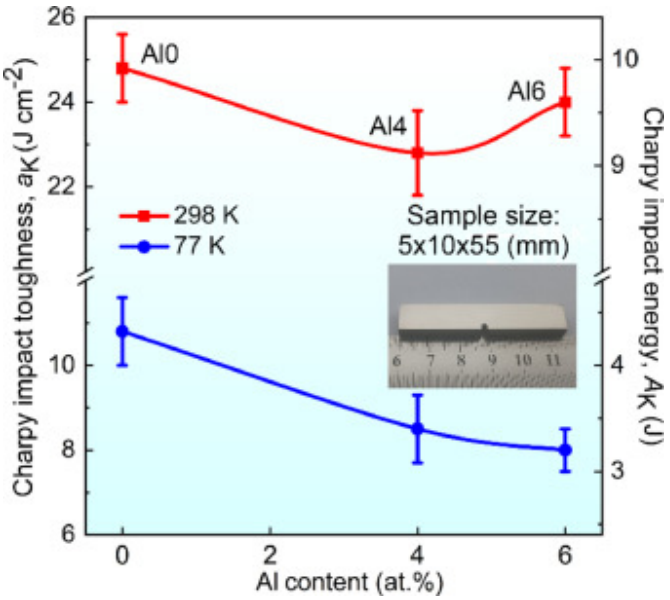

1. Download: Download high-res image (202KB)
2. Download: Download full-size image

Fig. 3. Charpy impact toughness and impact energy of Al*x* BMGCs at 298 and 77 K temperatures. The inset shows a typical image of the large-sized samples used for testing.

Table 2. Charpy impact toughness, a_K, and impact energy, A_K, of the studied BMGCs. The sample size, notch type and depth, and testing temperature are also listed.

BMGCs	Sample size (mm)	Notch type and depth (mm)	Temperature (K)	a_K(J cm^{-2})	A_K (J)
Al0	5 × 10 × 55	U, 2	298	24.8 ± 0.8	9.9 ± 0.3
			77	10.8 ± 0.8	4.3 ± 0.3
Al4	5 × 10 × 55	U, 2	298	22.8 ± 1.0	9.1 ± 0.4
			77	8.5 ± 0.8	3.4 ± 0.3
Al6	5 × 10 × 55	U, 2	298	24.0 ± 0.8	9.6 ± 0.3
			77	8.0 ± 0.5	3.2 ± 0.2
Al0–10C	5 × 10 × 55	U, 2	298	24.8 ± 1.0	9.9 ± 0.4
			77	9.8 ± 0.5	3.9 ± 0.2
Al0–30C	5 × 10 × 55	U, 2	298	26.0 ± 1.0	10.4 ± 0.4
			77	8.8 ± 0.8	3.5 ± 0.3

SEM images of the cracking paths in the Al0 samples fractured at 298 and 77 K are shown in Fig. 4(a, b), respectively. While cracks are observed in both, the one tested at 298 K has more tortuous cracks than that in the latter. SEM micrographs of the deformed regions in the specimens fractured at 298 and 77 K are presented in Fig. 4(c, d), respectively. A high density of martensitic laths inside β-Ti crystals, which block the propagation of shear

bands in the glassy ligaments, can be observed in Al0 tested at 298 K. In comparison, the numbers of martensitic laths and shear bands are much lesser in Al0 tested at 77 K. Moreover, shear bands in the latter cut across the dendrites. These observations are further confirmed in Fig. 4(e), where a comparatively larger amount of α″-Ti martensitic laths and α″-Ti twins, as identified by the SAED patterns (Fig. 4(f)), exist in the Al0 tested at 298 K than that tested at 77 K, as seen in Fig. 4(g, h). This implies that a greater extent of DIMT in Al0 occurs at 298 K during impact loading.

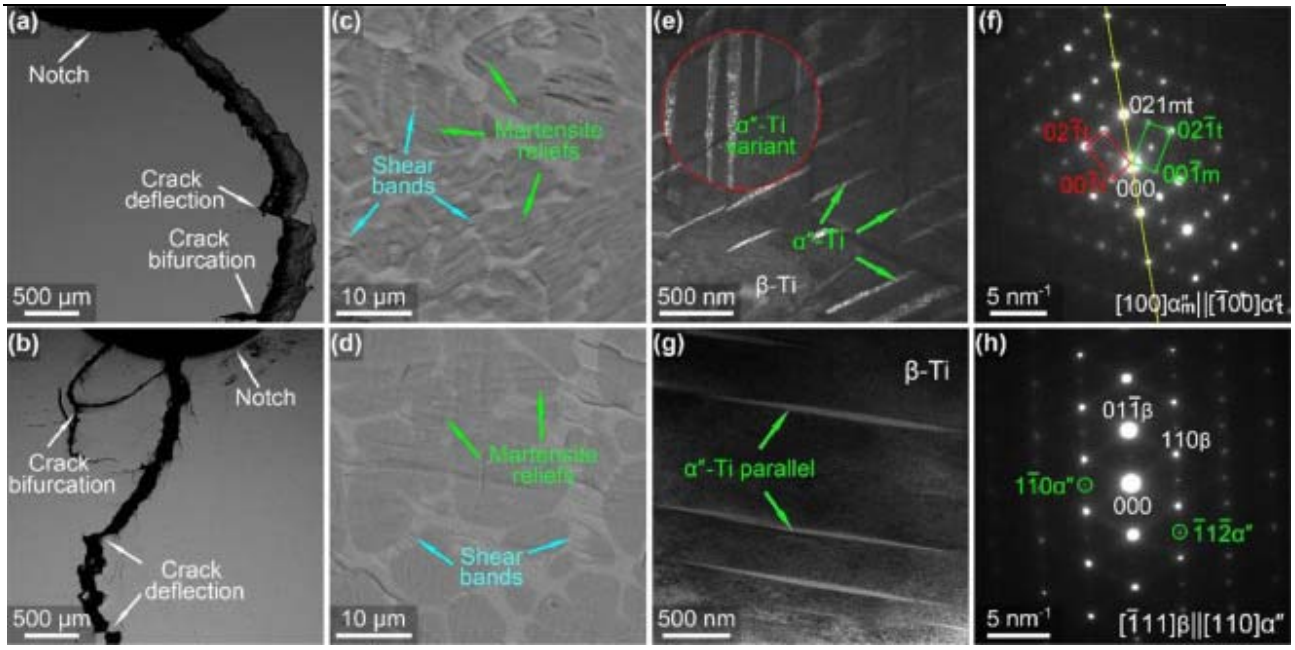

1. Download: Download high-res image (686KB)
2. Download: Download full-size image

Fig. 4. (a, b) Local side-view of the fractured Al0 at 298 and 77 K, respectively. (c, d) Magnified SEM micrographs next to the major crack at ~1.5 mm ahead of the notch, (e, g) TEM micrographs, and (f, h) SAED patterns of the fractured Al0 at 298 and 77 K, respectively.

The microstructures of Al6, tested at 298 and 77 K are shown in Fig. 5(a, b), respectively. As was seen for Al0, Al6 tested at 298 K exhibits a more tortuous cracks path and a ragged fracture surface (Fig. 5(a)) compared to that in the latter. However, more microcracks can be observed in Al6 samples than in Al0 samples that were tested at 77 K (Figs. 4(b) and 5(b)). Fig. 5(c, d) shows the magnified SEM images of the deformed areas around the cracks. While the β-Ti dendrites of Al6 samples tested at both temperatures also contain several martensitic laths, they are much lesser than that seen in Al0. In fact, β-Ti dendrites in Al6 that were tested at 77 K contains the least number of martensitic laths. Also, although a high density of shear bands cutting across both the glass matrix and β-Ti crystals was observed in Al6 tested at 298 K, only a few shear bands are observed in Al6 tested at 77 K. In fact, in the latter, some of the shear bands have evolved into cracks. A TEM image of the plastically deformed regions close to the cracks in Al6, tested at 298 K, is shown in Fig. 5(e). Thin α″-Ti laths in β-Ti crystals are observed, which further confirms that DIMT takes place during impact loading at this

temperature. Fig. 5(f) reveals that the orientation relationship between α″-Ti martensite and β-Ti parent phase is $[1\_11]_{\beta}//[110]_{\alpha''}$ and $(01\_1)_{\beta}//(002\_)_{\alpha''}$ [29,34]. In Fig. 5(g), the TEM micrograph of Al6 tested at 77 K is shown. A few α″-Ti laths, which are observed in these dendrites indicate that impact loading also induces DIMT in Al6 at 77 K. However, in this case, the corresponding SAED pattern in Fig. 5(h) reveals that the α″-Ti martensite and β-Ti parent phase have the $[100]_{\beta}//[100]_{\alpha''}$ and $(01\_1\_)_{\beta}//(020)_{\alpha''}$ orientation relationship [55].

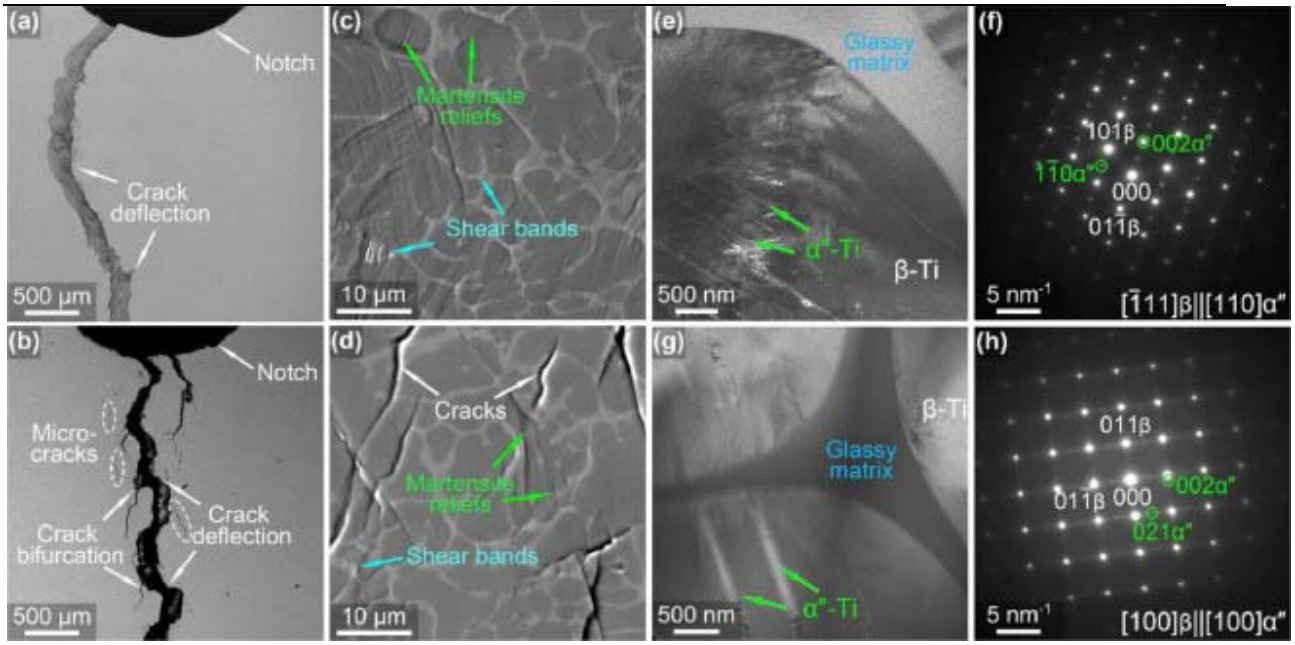

1. Download: Download high-res image (663KB)
2. Download: Download full-size image

Fig. 5. (a, b) Local side-view of the fractured Al6 at 298 and 77 K, respectively. (c, d) Magnified SEM micrographs next to the major crack at ~1.5 mm ahead of the notch, (e, f) TEM micrographs, and (g, h) SAED patterns of the fractured Al6 at 298 and 77 K, respectively.

The representative fracture surfaces of the Al*x* BMGCs that were impact tested at 298 and 77 K are shown in Figs. S4 and S5, respectively. In both samples, there are two distinct fracture morphologies that are the stable crack extension zone (near the notch tip) and the unstable crack extension zone (away from the notch tip). The unstable crack extension zone is composed of rough pits and dimples, while the stable crack extension zone is relatively flat and has vein-like features. The magnified SEM micrographs in Figs. S4(d-f) and S5(d-f) display that the stable crack extension zones contain vein patterns, which signify the onset of fluid meniscus instability (FMI) within cracks [17,56]. The characteristic widths, ΔW, of the FMI zones are related to the size of plastic zone ahead of the crack tip and play an important role in crack extension. The vein patterns on fracture surfaces of Al0, Al4, and Al6, impact tested at 298 K, have ΔW ~1090 μm, ~530 μm, and ~880 μm (Fig. S4(a-c)). This implies that the extent of plastic deformation is highest in Al0, followed by that in Al6 and then in Al4. Similarly, in impact-tested samples at 77 K, ΔW of Al0, which is ~570 μm, is also the highest, which is

followed by that of Al4 (~470 μm) and then that of Al6 (~330 μm) (Fig. S5(a-c)). The observed trends in the variations of the sizes of plastic zones and their a_K, with increasing Al content in the BMGCs, match closely.

3.3. Microstructures of the cryogenic cycle treated Al0 BMGCs

The microstructures of the cryogenic cycle treated Al0 BMGCs are shown in Fig. 6. The XRD patterns of the Al0–10C and Al0–30C are almost identical to the untreated Al0 (Fig. 6(a)), indicating that no additional phases form during the CCT and the glass matrix remains amorphous. By carefully comparing the morphology, size, and volume fraction of the dendrites in the SEM micrographs of Al0–10C and Al0–30C (Fig. 6(b, c)) with that of as-cast Al0, no noticeable change could be noted. Moreover, the compositional analysis of both the glass matrix and the dendrites are also identical to that of the BMGC in the as-cast state, as shown in Fig. S6 and listed in Table 1, which indicates that CCT does not cause compositional changes in either phase. Fig. 7 compares the EBSD results of Al0–30C with Al0. As can be seen from the phase map (Fig. 7(a)) and IPF color map (Fig. 7(b)), the precipitation of α″-Ti is not promoted in Al0 subjected to 30 CCT numbers, as the volume fraction of α″-Ti is only ~1.5%, which is identical to that in the as-cast Al0. In addition, the two phases of α″-Ti and β-Ti within the blue circle in Fig. 7(a) were analyzed and it was determined that their common orientation relationship of $[01\_1]_{\beta}//[001\_]_{\alpha''}$ and $(011)_{\beta}//(02\_0)_{\alpha''}$, also remains unaltered. This suggests that CCT neither affects the dendrite orientation nor the crystallographic relationship between β-Ti and α″-Ti, as seen in Fig. 7(b, c). The kernel average misorientation (KAM) maps of Al0 and Al0–30C are displayed in Fig. 7(d, e), respectively. The average KAM values (KAM_{AVE}) of β-Ti crystals in the as-cast Al0 and the Al0–30C are very similar, as seen in the insets of Fig. 7(d, e), which indicates that 30 CCT numbers do not lead to significant lattice distortion or induce dislocations in the β-Ti crystals.

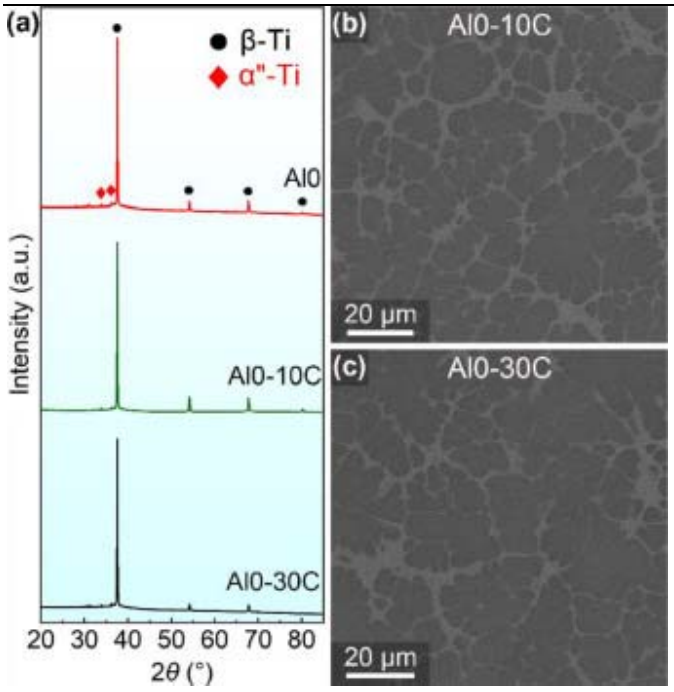

1. Download: Download high-res image (315KB)
2. Download: Download full-size image

Fig. 6. (a) XRD patterns, (b, c) SEM micrographs of the Alo–10C and Alo–30C BMGCs, respectively.

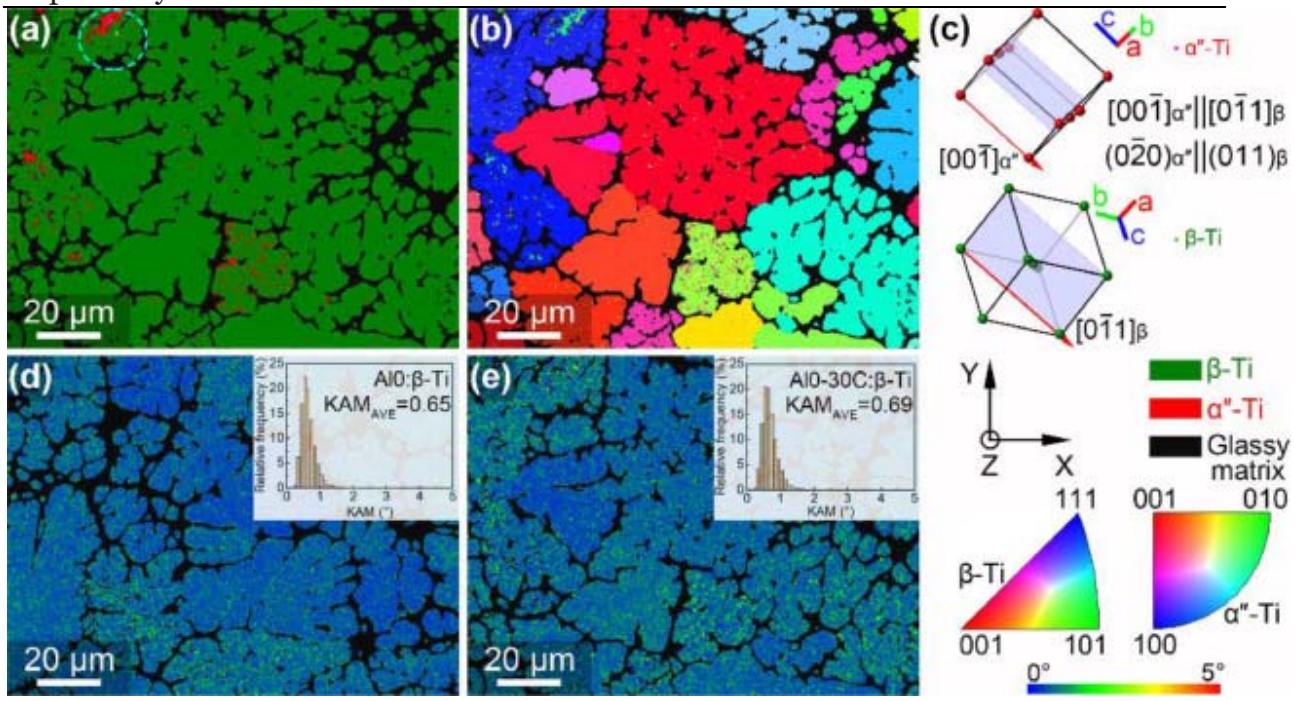

1. Download: Download high-res image (1MB)
2. Download: Download full-size image

Fig. 7. (a, b) Phase maps and IPF color maps of the Alo–30C BMGC, respectively. (c) The schematic diagram of the crystallographic orientation relationship between the two phases in the blue circle in (a) and the color bars of (a, b). (d, e) KAM maps of the as-cast Alo and Alo–30C BMGCs, respectively, with the insets showing the corresponding histogram of KAM statistics.

Next, DSC was performed on the as-cast and CCT-treated Alo samples to investigate the energy states of their corresponding glass phases. Fig. 8 shows the DSC scans of the as-cast Alo, Alo–10C, and Alo–30C. During the heating, of all the three BMGCs, an exothermic event arising from $\beta \rightarrow \beta + \omega$ transition [52], an endothermic region corresponding to the glass transition, followed by a supercooled liquid region and exothermic peaks of crystallization were observed. The enlarged relaxation stages (before T_g) are shown in the inset of Fig. 8. Although they have similar characteristic temperatures, there are differences in the relaxation enthalpy, ΔH_{rel}, of the glass matrix, which is the energy difference between different states and is often used as quantitative measurements of the structural state of glasses [57,58]. It has been found that the average ΔH_{rel} increases with the number of cycles, from 10.77 ± 0.53 J g^{-1} of Alo to 11.12 ± 0.72 J g^{-1} of Alo–10C to 12.48 ± 0.86 J g^{-1} of Alo–30C. It is noteworthy that the measured $\Delta H_{rel.}$ values include the released heat of $\beta \rightarrow \beta + \omega$. However, considering the fact the CCT does not alter the compositions and volume fraction of β-Ti crystals (Figs. 6 and 7) and the KAM maps in Fig. 7, the thermal stress of CCT can hardly affect the ω-Ti transition, and it is reasonably to infer that the amount and heat release of $\beta \rightarrow \beta + \omega$ are similar in

the three BMGCs. Therefore, the changes in the measured $\Delta H_{rel.}$ intrinsically measures the variations in the energy states of the glass matrices in the BMGCs. A higher $\Delta H_{rel.}$ indicates a less relaxed state of the glassy phase [57,58], which implies that 10 and 30 cycles of CCT have a rejuvenating effect on the Al0 BMGC.

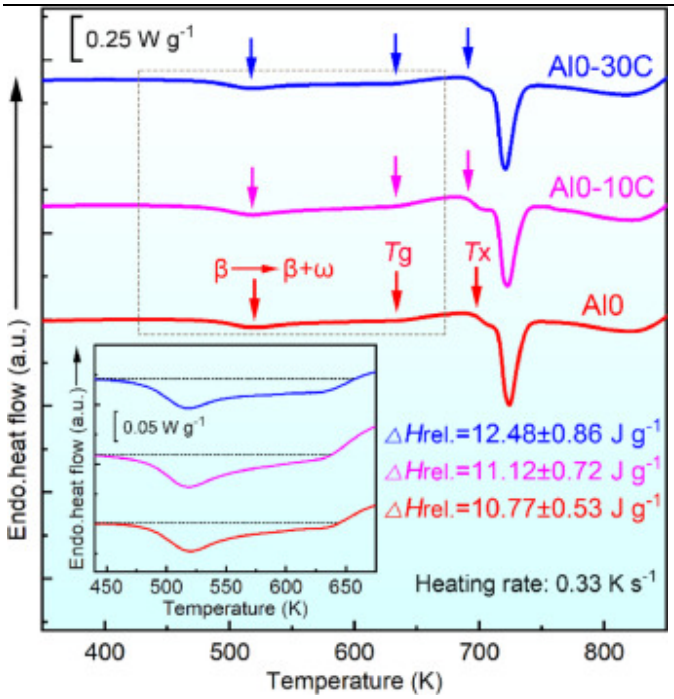

1. Download: Download high-res image (363KB)
2. Download: Download full-size image

Fig. 8. DSC traces of the cryogenic cycle treated Al0 BMGC plates. The inset shows the enlarged traces before T_g for measuring the relaxation enthalpies.

3.4. Impact toughness and fractured microstructures of cryogenic cycle treated Al0 BMGCs

Fig. 9 shows the variations of the measured impact toughness, a_K, and impact energy, A_K, of the as-cast Al0, Al0–10C, and Al0–30C tested at 298 and 77 K. The inset of Fig. 9 shows the schematic process diagram of CCT used in this work. At 298 K, while Al0 and Al0–10C have similar a_K of 24.8 ± 0.8 and 24.8 ± 1.0 J cm^{-2}, respectively, that of Al0–30C is 26.0 ± 1.0 J cm^{-2}. In contrast, a_K at 77 K of Al0 decreases with increasing numbers of CCT. The a_K of Al0, Al0–10C, and Al0–30C are ~10.8 ± 0.8, 9.8 ± 0.5, and 8.8 ± 0.8 J cm^{-2}, respectively.

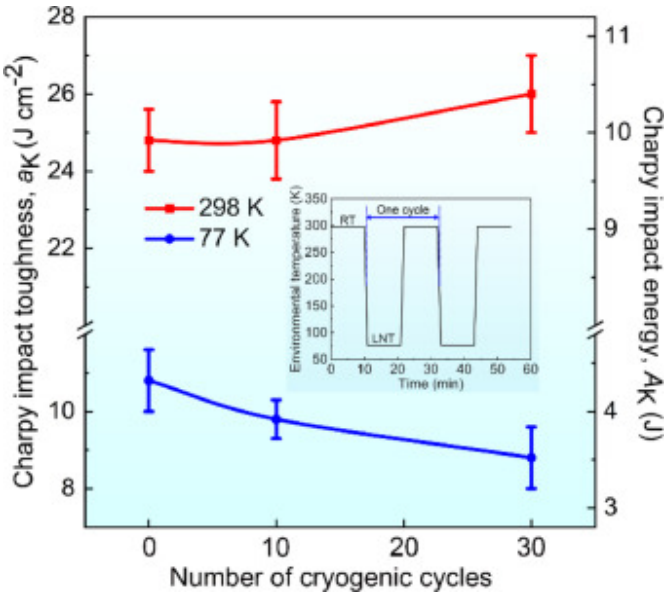

1. Download: Download high-res image (198KB)
2. Download: Download full-size image

Fig. 9. Charpy impact toughness and impact energy of the Al0 BMGC with CCT at 298 and 77 K. The inset shows a schematic of the CCT process.

Fig. 10(a, b) shows the side surfaces of Al0–30C that were impact tested at 298 and 77 K, respectively. At 298 K, the cracks are tortuous and only a few microcracks form alongside the major crack. In contrast, although crack deflection and bifurcation also can be seen in the specimen tested at 77 K, many microcracks form near the major crack. Fig. 10(c, d) shows the deformed regions near the major cracks of Al0–30C tested at 298 and 77 K, respectively. A high density of martensitic laths inside β-Ti crystals and shear bands within the glassy ligaments are observed in Al0–30C tested at 298 K, indicating severely plastic deformation of β-Ti crystals and the glass matrix. In comparison, only a few martensitic laths and shear bands are also observed in Al0–30C tested at 77 K. Moreover, some of these shear bands have also evolved into cracks. The TEM micrographs of the Al0–30C specimens tested at 298 and 77 K are shown in Fig. 10(e, f), respectively. A high density of α″-Ti martensitic plates, as well as its twins with different orientations, are presented in Al0–30C tested at 298 K but not those many were observed in that tested at 77 K, which confirms the substantial occurrence of DIMT of β-Ti → α″-Ti during its impact deformation in the former. The α″-Ti martensite in Al0–30C tested at 298 K undergoes mechanical twinning by shearing on the lattice plane of $(111\_)_{\alpha''}$ [59], as observed in the SAED pattern in the zone axis of $[101]_{\alpha''}$, as shown in Fig. 10(g). In contrast, the few α″-Ti martensitic plates found in Al0–30C tested at 77 K, have a crystallographic orientation of $[1\_11]_{\beta}//[110]_{\alpha''}$ and $(011\_)_{\beta}//(002\_)_{\alpha''}$ with the parent β-Ti phase in the zone axis of $[1\_11]_{\beta}$ (Fig. 10(h)).

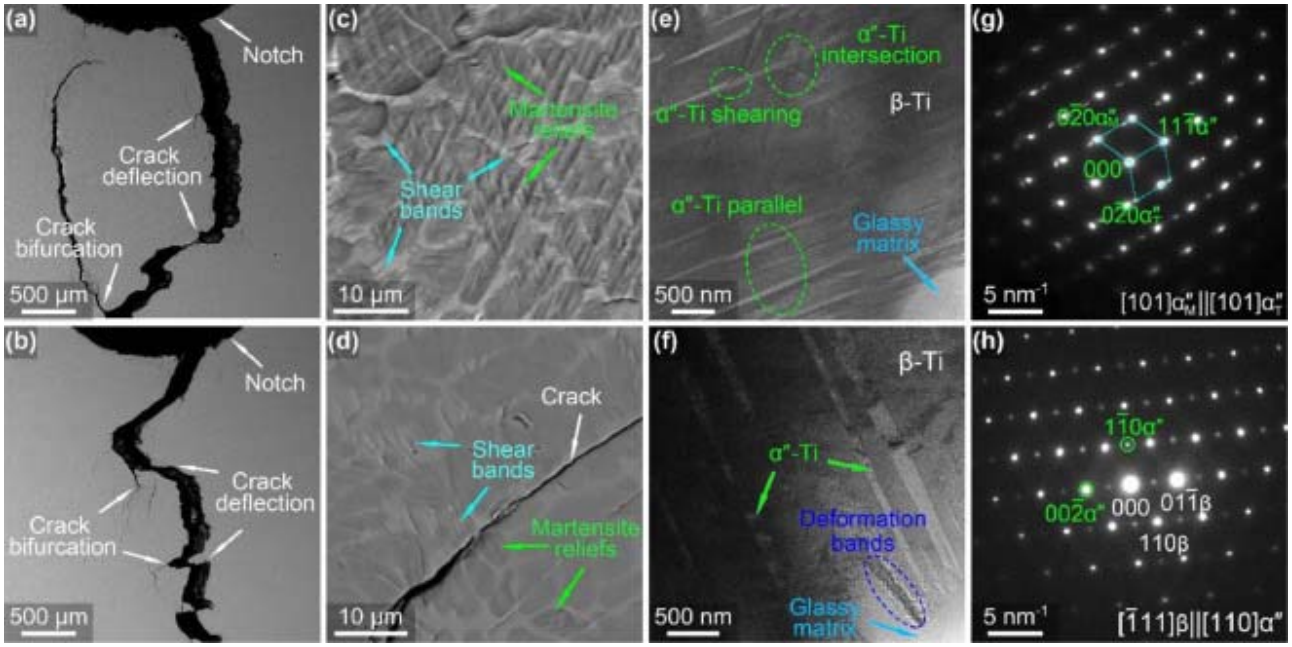

1. Download: Download high-res image (751KB)
2. Download: Download full-size image

Fig. 10. (a, b) Local side-view of the fractured Alo–30C at 298 and 77 K, respectively. (c, d) Magnified SEM micrographs next to the major crack at ~1.5 mm ahead of the notch, (e, f) TEM micrographs, (g, h) SAED patterns of the fractured Alo–30C at 298 and 77 K, respectively.

The fracture surfaces near the notch tip regions of Alo–30C, impact tested at 298 and 77 K, are shown in Fig. S7 (a, b), respectively. As seen earlier in the as-cast Alo (Fig. S4), the fracture surfaces of Alo–30C tested at 298 K are rougher, more uneven, and have a higher density of dimples and vein patterns, than that tested at 77 K. The ΔW of the FMI zone in Alo–30C tested at 298 K is ~1220 μm whereas that tested at 77 K is only ~500 μm. Note that the corresponding fracture surfaces of as-cast Alo tested at 298 and 77 K have slightly lower ΔW.

4. Discussion

4.1. Temperature dependence of transformation toughening in BMGCs

The DIMT of β-Ti dendrites in phase-transformable BMGCs operates by long-range lattice shear with large shear strains, but the DIMT of crystals in BMGCs is confined by the surrounding continuous glass matrix, which is very different from the case of DIMT of free-standing single-crystal or polycrystalline states [30,[60], [61], [62]]. Understanding the DIMT of confined crystals in BMGCs is vital for revealing the transformation toughening mechanisms in BMGCs. It has been reported earlier that metastable β-Ti crystals in Ti-based BMGCs do not undergo β-Ti → α″-Ti transformation when the temperature decreases to 77 K without external forces due to the strong confinement of the glass matrix [30]. However, the metastable β-Ti crystals in Ti-based BMGCs can still undergo DIMT under applied load, because stress can partially overcome the confinement offered by the matrix [30]. Since the strength of the glass matrix increases with decreasing temperatures, the confinement effect exerted on crystals by the glass matrix becomes more pronounced at low temperatures, such as at 77 K, which limits the DIMT of crystals [31]. This phenomenon has been also confirmed during the tribological testing of a phase-transformable Ti-based BMGC, in which the DIMT of β-Ti crystals was suppressed at cryogenic temperatures [63].

In order to reveal the confinement effect of the matrix on DIMT of BMGCs at different temperatures, the EBSD maps of the fractured Al0 at 298 and 77 K are shown in Fig. 11. At 298 K, a high fraction of β-Ti dendrites transforms into α″-Ti martensite (Fig. 11(a)). In addition, many variants of α″-Ti (marked with different colors in the same dendrites in Fig. 11(b)) with different orientations form, which can effectively accommodate large plastic strains and contribute to energy absorption during impact [64], [65], [66]. Fig. 11(c) shows the KAM map of Al0 impact-tested at 298 K. It is found that the local misorientation level of β-Ti and α″-Ti is similar, indicating that both the β-Ti and α″-Ti phase uniformly share the plastic strains [67,68]. In comparison, only a small amount of DIMT of β-Ti crystals takes place during impact loading of Al0 at 77 K, as shown in Fig. 11(d), and only a few and small α″-Ti variants forms in the regions with high local strains, such as those near cracks (Fig. 11(e)). The KAM map of Al0 tested at 77 K is shown in Fig. 11(f). It is obvious that the KAM value of α″-Ti martensite is significantly higher than that of β-Ti, which contrasts with that observed at 298 K, suggesting that the plastic deformation is uneven and concentrated in the regions with α″-Ti martensite [67,68]. Figs. 11(g) shows plots of relative fractions of the two crystalline phases in as-cast Al0 that were impact tested at 298 and 77 K. The fraction of α″-Ti in Al0 impact tested at 298 K is ~79.2% (percentage of the crystalline phases) but in that tested at 77 K it is only ~12.48% (Fig. 11(g)), which confirms the enhanced restraint on DIMT by the glass matrix at lower temperatures as mentioned above [30,34]. Fig. 11(h) shows the plots of geometrical necessary dislocation (GND) density in β-Ti and α″-Ti in the as-cast Al0 specimens that were tested at 298 and 77 K. For as-cast Al0 that was tested at 298 K, the GND density in β-Ti and α″-Ti are quite similar and in the range of ~ 2.58–2.62 × 10^{16} m^{-2}. However, in the as-cast Al0, which was impact tested at 77 K, the GND in the β-Ti and α″-Ti phases dramatically reduces to 1.43 × 10^{16} and 2.18 × 10^{16} m^{-2}, respectively. Therefore, the amount of DIMT and the plastic deformability of crystals in

phase-transformable BMGCs are strongly dependent on the testing temperatures, which play a vital role in activating the transformation induced toughening of BMGCs. At 298 K, the toughness of the dendrites, which absorb energy during DIMT, is the primary toughening mechanism of the BMGC [30,68,69]. In contrast, the strong confinement effect on DIMT by the glass matrix at 77 K limits transformation induced toughening of dendrites, and hence the toughness of the BMGC is governed by the toughness of the glass matrix [22].

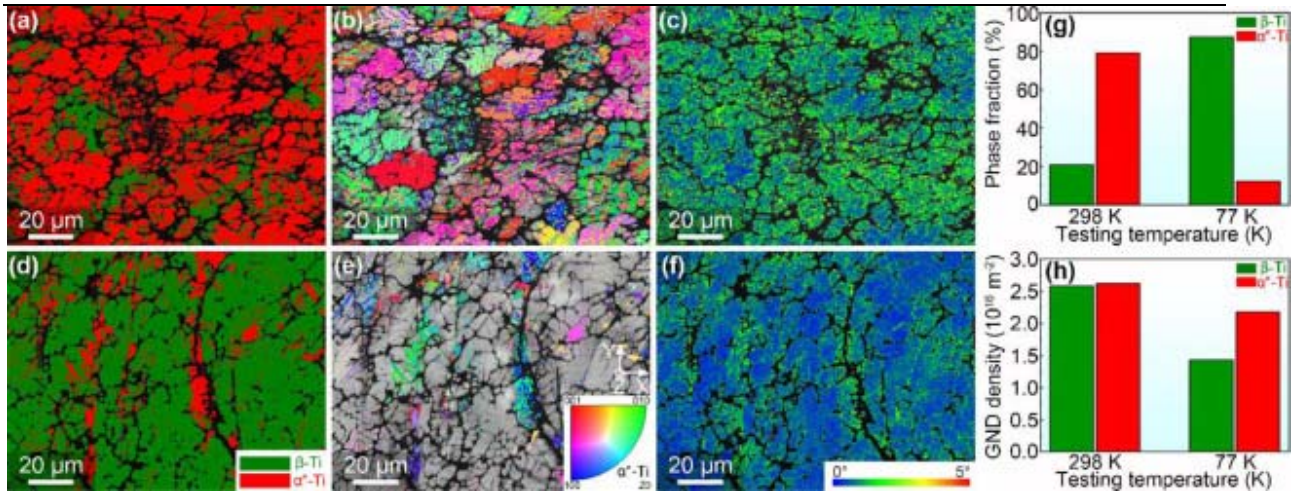

1. Download: Download high-res image (1MB)
2. Download: Download full-size image

Fig. 11. (a–c) Phase map, α″-Ti IPF color map and KAM map of the fractured Alo at 298 K, respectively. (d–f) Phase map, α″-Ti IPF color map, and KAM map of the fractured Alo at 77 K, respectively. (g) Statistical graph of the β-Ti and α″-Ti mutual volume fraction in the fractured Alo at 298 and 77 K. (h) GND density in the β-Ti and α″-Ti phases in the fractured Alo at 298 and 77 K, respectively.

4.2. Effects of Al addition on impact toughness of phase-transformable BMGCs

It has been demonstrated earlier that the impact toughness of phase-transformable BMGCs depends on the operation of DIMT [30,34]. However, the effects of tuning phase metastability, which is the intrinsic factor governing DIMT, on the impact toughness of phase-transformable BMGCs are not fully understood. Typically, Al is expected to stabilize α-Ti, which reduces the phase stability of β-Ti [27,70]. However, for BMGCs with a glass matrix and β-Ti dendrites, the Al addition alters the contents of other elements in both phases, and it has been found that Al addition up to 8 at.% can incrementally increase the phase stability of β-Ti crystals in a BMGC, when Cu, a β-Ti stabilizing element, is dissolved in the crystals [28]. Therefore, whether Al addition increases or decreases the phase stability of β-Ti phases in BMGCs should be carefully analyzed on a case-to-case basis. In addition, it has been widely accepted that the crystal size also significantly affects the ease and density of DIMT of the crystals, and it is much more difficult for fine crystals to undergo DIMT than coarse ones [26,29,34]. Moreover, it has been reported that the addition of Al forms covalent-like bonds in metallic glasses,

which enhances their strength and hardness but deteriorates the toughness of the glass phase [28,[71], [72], [73]]. Therefore, the addition of Al addition to phase-transformable BMGCs may involve a trade-off in the terms of obtaining the optimum toughness of the matrix and the dendrites.

In the current Al*x* BMGCs, it is observed that the phase stability of β-Ti in Al0 and Al4 are the lowest and highest, respectively. In Al6, the β-Ti phase stability is intermediate of the two, as confirmed by TEM and DSC results (Figs. 1 and S2). The phase stability of β-Ti determines the ease and extent of DIMT in β-Ti, which fundamentally contributes to the toughness of BMGCs. Moreover, it is worth noting that temperature is an additional parameter that influences the stability of β-Ti stability, which in turn affects a_K of phase-transformable BMGCs. The fundamental mechanisms that govern the toughness of the current Al*x* BMGCs at different temperatures are schematically shown in Fig. 12. As mentioned earlier, the phase-transformable BMGCs consist of a glass matrix as well as the phase-transformable β-Ti crystals. Under impact loading, the shear deformation of the glass matrix and transformation toughening of β-Ti synergistically accommodate the large plastic deformation of BMGCs while resisting the crack extension. Consequently, the a_K of the current Al*x* BMGCs is determined by the toughness of both the glass matrix and β-Ti. The toughness of the latter is closely related to the stability of β-Ti, which determines the critical stress for initiating the phase transformation. Since both the plastic deformation of the matrix and stability of β-Ti are highly sensitive to temperature, the interplay between could vary significantly with temperature. At 298 K, a_K is sensitive to the phase stability and the extent of DIMT in β-Ti dendrites dominates, which is corroborated by the fact that increasing the Al content in β-Ti from 0 to 4 at.% in Al*x* alloys stabilizes the dendrites but decreases a_K at 298 K. With further 6 at.% Al addition, the β-Ti phase becomes metastable again, and the extent to which it undergoes DIMT increases, which in turn increases its a_K. In comparison, as the testing temperature decreases to 77 K, the extent of DIMT significantly decreases due to the strong confinement by the glass matrix at the extremely low temperature. Therefore, the contribution of the transformation of crystals is minimal and the intrinsic toughness of the glass matrix governs the overall toughness of the BMGC. Since Al addition causes the formation of more covalent-like bonds in the glass matrix increasing its content can embrittle the glass matrix. This explains the decreasing trend of a_K with increasing Al content in the Al*x* BMGCs at 77 K. Note that the finer β-Ti secondary dendritic arms in Al4 and Al6, compared to that in Al0, also limits DIMT in them, which is an additional cause of the above-mentioned trend in a_K.

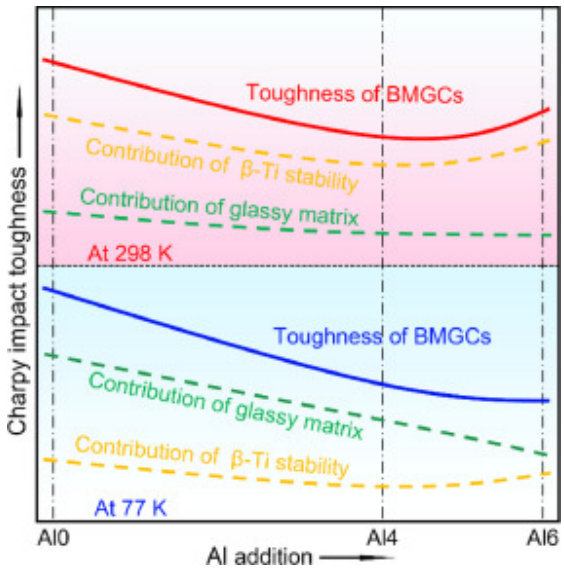

1. Download: Download high-res image (280KB)
2. Download: Download full-size image

Fig. 12. The schematic diagram showing the different effects of Al addition on impact toughness for phase-transformable BMGCs at 298 and 77 K, respectively.

4.3. Effects of cryogenic cycle treatment on impact toughness of phase-transformable BMGCs

It has been widely reported that CCT can increase the free volume content and elevate the energy states of the glass phase after a certain number of cryogenic cycles, which are effective in enhancing the deformability and toughness of BMGs and BMGCs at 298 K [39,40,42,46,58,74,75]. Similarly, CCT is expected to increase the free volume of the glass matrix in BMGCs and can hence be applied for toughening it. For the current BMGCs, DSC measurements show that $\Delta H_{rel.}$ increases after 30 times of CCT, which implies that the BMGC has a higher free volume and is at a higher energy state. The increase in free volume content and the elevation of energy state not only promotes the nucleation of multiple shear bands but also softens the glass matrix [39,42,74]. Therefore, the confinement of DIMT of crystal by the glass matrix is expected to be lower in BMGCs whose matrix has been CCT cycled to a state having greater free volume. This argument is supported by the observation that the volume fraction of α″-Ti martensite in Al0–30C is ~94.5%, which is significantly higher than that of as-cast Al0 during impact testing (Figs. 11(a) and 13(a)). As shown in Fig. 13(b, c), CCT does not significantly affect the orientations and strain distribution of the dendrites in Al0–30C tested at 298 K, which indicates that a larger amount of phase transformation can absorb more impact energy.

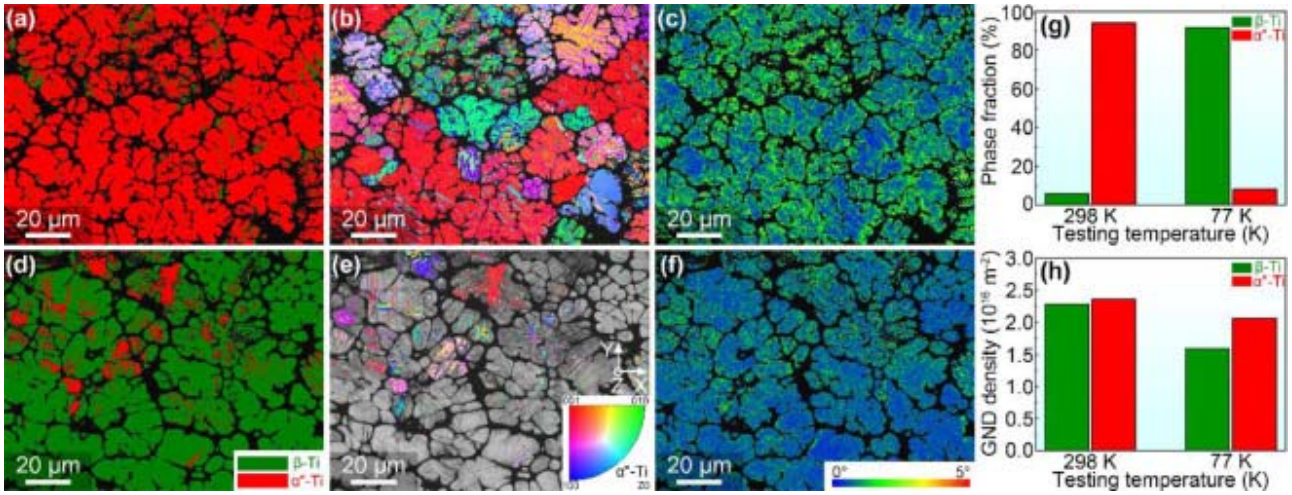

1. Download: Download high-res image (1MB)
2. Download: Download full-size image

Fig. 13. (a–c) Phase map, α″-Ti IPF color map and KAM map of the fractured Alo–30C at 298 K, respectively. (d–f) Phase map, α″-Ti IPF color map, and KAM map of the fractured Alo–30C at 77 K, respectively. (g) Statistical graph of β-Ti and α″-Ti mutual volume fractions in the fractured Alo–30C at 298 and 77 K. (h) GND density in β-Ti and α″-Ti phases in the fractured Alo–30C at 298 and 77 K, respectively.

Based on this discussion, the variations of a_K of the CCT-treated BMGCs, tested at 298 K, are along the expected lines. After 30 CCT numbers, the rejuvenation of the glass matrix not only improves the toughness of the matrix in Alo–30C, but also relieves the confining effect on dendrites by the matrix, which leads to more profuse DIMT in them, which in turn enhances the a_K of Alo–30C compared to that of the as-cast Alo. Alternately, Alo–10C possesses a similar a_K as the untreated Alo, as the glass matrix in Alo–10C is probably not sufficiently rejuvenated to alleviate the confinement effect by the glass matrix on the dendrite. This is supported by the observation that the extent of DIMT in dendrites of Alo–10C and Alo is similar.

On increasing the number of CCT cycles, the a_K at 77 K of the BMGCs continuously decreases, which is different than the trend observed at 298 K. Fig. 13(d–f) shows that the volume fraction of α″-Ti martensite in impact tested Alo–30C is ~8.25% BMGCs, which is slightly lower than that of Alo by ~4%, at 77 K. Note that the difference in orientation relationships and dislocation density in the two phases is not significant. In Fig. 13(g, h), the variations in the phase fractions of α″-Ti and β-Ti in Alo–30C that were impact-tested at 298 and 77 K are displayed. This further confirms that Alo–30C undergoes greater plastic deformation via DIMT compared to that in Alo at 298 K, but the trend reverses at 77 K. It has been demonstrated that structural and property changes in BMGs and BMGCs treated with CCT are associated with local atomic rearrangements caused by the non-affine thermal expansion-contraction at the nano-scale arising from the intrinsic heterogeneity itself [38,74,76,77]. Moreover, it has been reported that the rejuvenation of glass phases by CCT softens the hard regions without affecting the already soft regions [38,42]. The role of soft regions in metallic glasses is to promote the formation of shear bands and hard regions are to hinder or deflect shear band propagation. These mechanically heterogeneous regions in metallic glasses can effectively prevent the rapid

evolution of shear bands into cracks and improve the plasticity [38,42,[78], [79], [80]]. After CCT, the hard regions in the glass matrix soften, and soft regions facilitate the activation of shear transformation zones (STZs) and the formation of shear bands at 298 K, which together with the DIMT of crystals contribute to the high a_K of Al0–30C at 298 K. However, at 77 K, the uniform soft regions of the rejuvenated glass matrix become uniform hard regions due to the temperature effect, which are incapable of blocking shear bands during plastic deformation and lead to greater plastic strain localization in it than that in as-cast Al0. As a result, the shear bands in Al0–30C transform into cracks faster, which leads to its embrittlement at 77 K compared to its as-cast counterpart. Note that, as discussed earlier, the intrinsic toughness of the glass matrix dominates the toughness of BMGCs at 77 K, as the constraint imposed by the hard matrix makes the dendrites more resistant to DIMT. Therefore, increasing the CCT cycles deteriorates a_K at 77 K in the phase-transformable BMGCs. These results indicate that the rejuvenation of the glass matrix can affect the toughness of BMGCs at 298 and 77 K in contrasting ways.

5. Conclusions

In summary, the effects of Al addition and CCT on the Charpy impact toughness, a_K, at 298 and 77 K of Ti-based BMGCs containing phase-transformable β-Ti crystals are thoroughly investigated and the fundamental mechanisms are analyzed and discussed in this work. The main findings are summarized as follows:

1) The glass matrix limits the DIMT of β-Ti crystals in BMGCs. Moreover, since the strength and hardness of the glass matrix increase with decreasing temperature, DIMT in the dendrites is significantly inhibited at 77 K. Consequently, the impact toughness of the BMGCs at 298 K is sensitive to the extent of DIMT, whereas at 77 K it is mainly determined by the intrinsic toughness of the glass matrix.
2) With Al addition, the average span length of the entire β-Ti dendrites increases but the size of secondary dendritic arms decreases. The phase stability of β-Ti gets tuned by Al addition, such that is the lowest in Al0 but the highest in Al4. At 298 K, the a_K first decreases from Al0 to Al4 and then increases again to Al6, which is mainly dominated by the β-Ti phase stability and the amount of DIMT. At 77 K, the impact toughness of the Alx BMGCs monotonically decreases with the increase in the Al content. It was revealed that the intrinsic toughness of the glass matrix determines the toughness of the BMGCs at 77 K. Since the addition of Al in the BMGC forms more covalent-like bonds in the glass matrix, its increased content leads to embrittlement at 77 K.
3) CCT can effectively rejuvenate the matrix of phase-transformable Al0 BMGC. After 30 times of CCT, the Al0–30C exhibits a much higher a_K than as-cast Al0. This can be attributed to the rejuvenated glass matrix and a larger amount of DIMT due to the softening of the glass matrix. However, at 77 K, the a_K monotonically decreases with the increasing number of CCT cycles. This is because CCT induces a more mechanically uniform microstructure of the glass matrix, which becomes uniformly hard at 77 K and promotes strain localization and cannot effectively hinder the transformation of shear bands into cracks. Therefore, the rejuvenation of the glass matrix may have contrasting effects on the toughness of BMGCs at 298 and 77 K.

These findings not only reveal the fundamental deformation mechanisms during impact testing of phase-transformable BMGCs but also provide a vital guide for the development of BMGs and BMGCs with high-impact toughness.

Acknowledgments

This work was financially supported by the National Natural Science Foundation of China (Nos. 52171164 and 51790484), National Key Laboratory of Science and Technology on Materials under Shock and Impact (WDZC2022-13), the National Key Research and Development Program of China (No. 2021YFA0716303), Start-up research grant (No. SRG/2020/000095) of Science and Engineering Research Board, DST, GoI. A*STAR, Singapore via the Structural Metals and Alloys Program (No. A18B1b0061), the Natural Science Foundation of Liaoning Province (No. 2021-MS-009), the China Manned Space Engineering, the Chinese Academy of Sciences (ZDBS-LY-JSC023), and the Youth Innovation Promotion Association CAS (No. 2021188).

Appendix. Supplementary materials

Download: Download Word document (4MB)

References

[1]

W.H. Wang

Prog. Mater. Sci., 106 (2019), Article 100561

View PDFView articleView in ScopusGoogle Scholar
[2]

C. Schuh, T. Hufnagel, U. Ramamurty

Acta Mater., 55 (2007), pp. 4067-4109

View PDFView articleView in ScopusGoogle Scholar
[3]

A.L. Greer, E. Ma

MRS Bull., 32 (2007), pp. 611-615

CrossrefGoogle Scholar
[4]

B.A. Sun, W.H. Wang

Prog. Mater. Sci., 74 (2015), pp. 211-307

View PDFView articleView in ScopusGoogle Scholar
[5]

D. Raut, R.L. Narayan, P. Tandaiya, U. Ramamurty

Acta Mater., 144 (2018), pp. 325-336

View PDFView articleView in ScopusGoogle Scholar
[6]

R.L. Narayan, D. Raut, U. Ramamurty

Acta Mater., 150 (2018), pp. 69-77

View PDFView articleView in ScopusGoogle Scholar
[7]

R.L. Narayan, P.S. Singh, D.C. Hofmann, N. Hutchinson, K.M. Flores, U. Ramamurty

Acta Mater., 60 (2012), pp. 5089-5100

View PDFView articleView in ScopusGoogle Scholar
[8]

A. Bhattacharyya, G. Singh, K.E. Prasad, R. Narasimhan, U. Ramamurty

Mater. Sci. Eng. A-Struct. Mater. Prop. Microstruct. Process., 625 (2015), pp. 245-251

View PDFView articleView in ScopusGoogle Scholar
[9]

R. Qu, R. Maaß, Z. Liu, D. Tönnies, L. Tian, R.O. Ritchie, Z. Zhang, C.A. Volkert

Acta Mater., 218 (2021), Article 117219

View PDFView articleView in ScopusGoogle Scholar
[10]

C.C. Hays, C.P. Kim, W.L. Johnson

Phys. Rev. Lett., 84 (2000), pp. 2901-2904

View in ScopusGoogle Scholar
[11]

S. Pauly, G. Liu, G. Wang, U. Kuhn, N. Mattern, J. Eckert

Acta Mater., 57 (2009), pp. 5445-5453

View PDFView articleView in ScopusGoogle Scholar
[12]

Y. Wu, Y.H. Xiao, G.L. Chen, C.T. Liu, Z.P. Lu

Adv. Mater., 22 (2010), pp. 2770-2773

CrossrefView in ScopusGoogle Scholar
[13]

Z.J. Yu, W. Zheng, Z.Q. Li, Y.Z. Lu, X.B. Yun, Z.X. Qin, X. Lu

J. Mater. Sci. Technol., 78 (2021), pp. 68-73

View PDFView articleView in ScopusGoogle Scholar
[14]

D.C. Hofmann, J.Y. Suh, A. Wiest, G. Duan, M.L. Lind, M.D. Demetriou, W .L. Johnson

Nature, 451 (2008), pp. 1085-1089

CrossrefView in ScopusGoogle Scholar
[15]

L. Zhang, S. Pauly, M.Q. Tang, J. Eckert, H.F. Zhang

Sci. Rep., 6 (2016), p. 19235

View in ScopusGoogle Scholar
[16]

Z.Q. Liu, G. Liu, R.T. Qu, Z.F. Zhang, S.J. Wu

T. Zhang, Sci. Rep., 4 (2014), p. 4167

View in ScopusGoogle Scholar
[17]

D. Rajpoot, R.L. Narayan, L. Zhang, P. Kumar, H. Zhang, P. Tandaiya, U. Ramamurty

Acta Mater., 213 (2021), Article 116963

View PDFView articleView in ScopusGoogle Scholar
[18]

W. Hu, Z. Yu, Y. Lu, J. Huo, Z. Qin, X. Lu, R.L. Narayan

J. Alloy. Compd., 918 (2022), Article 165539

View PDFView articleView in ScopusGoogle Scholar
[19]

M.Q. Tang, H.F. Zhang, Z.W. Zhu, H.M. Fu, A.M. Wang, H. Li, Z.Q. Hu

J. Mater. Sci. Technol., 26 (2010), pp. 481-486

View PDFView articleView in ScopusGoogle Scholar
[20]

Y.Z. Lu, S. Su, S.B. Zhang, Y.J. Huang, Z.X. Qin, X. Lu, W. Chen

Acta Mater., 206 (2021), Article 116632

View PDFView articleView in ScopusGoogle Scholar

[21]

L., Zhang, H.F. Zhang, W.Q. Li, T. Gemming, Z.W. Zhu, H.M. Fu, J. Eckert , S. Pauly

Scr. Mater., 125 (2016), pp. 19-23

View PDFView articleView in ScopusGoogle Scholar
[22]

S. Roberts, C. Zachrisson, H. Kozachkov, A. Ullah, A.A. Shapiro, W.L. Johnson, D.C. Hofmann

Scr. Mater., 66 (2012), pp. 284-287

View PDFView articleView in ScopusGoogle Scholar
[23]

J.-.L. Gu, G.-.N. Yang, P. Gong, Y. Shao, K.-.F. Yao

Mater. Sci. Eng. A-Struct. Mater. Prop. Microstruct. Process., 786 (2020), Article 139442

View PDFView articleView in ScopusGoogle Scholar
[24]

D.C. Hofmann, P. Bordeenithikasem, Z. Dawson, L. Hamill, R.P. Dillon, B. McEnerney, S. Nutt, S.C. Bradford

Aerosp. Sci. Technol. (2018), pp. 513-519

82-83

View PDFView articleView in ScopusGoogle Scholar
[25]

H.Y. Li, Z. Wang, H.J. Yang, X.H. Shi, J.W. Qiao, H.P. Zhang, Y.C. Wu

Intermetallics, 126 (2020), Article 106877

View PDFView articleView in ScopusGoogle Scholar
[26]

Y.S. Oh, C.P. Kim, S. Lee, N.J. Kim

Acta Mater., 59 (2011), pp. 7277-7286

View PDFView articleView in ScopusGoogle Scholar
[27]

L. Zhang, Z.W. Zhu, H.M. Fu, H. Li, H.F. Zhang

Mater. Sci. Eng. A-Struct. Mater. Prop. Microstruct. Process., 689 (2017), pp. 404-410

View PDFView articleView in ScopusGoogle Scholar
[28]

J.H. Zhang, L. Zhang, H.W. Zhang, H.M. Fu, H. Li, H.F. Zhang

Scr. Mater., 173 (2019), pp. 11-15

View PDFView articleCrossrefGoogle Scholar
[29]

L. Zhang, R.L. Narayan, H.M. Fu, U. Ramamurty, W.R. Li, Y.D. Li, H.F. Zh ang

Acta Mater., 168 (2019), pp. 24-36

View PDFView articleView in ScopusGoogle Scholar
[30]

L. Zhang, J.H. Zhang, H.B. Ke, B.A. Sun, Z.W. Zhu, Y.D. Wang, H. Li, A.M . Wang, H.F. Zhang

Acta Mater., 222 (2021), Article 117444

Google Scholar
[31]

L. Zhang, H.F. Zhang, W.Q. Li, T. Gemming, P. Wang, M. Boenisch, D. So pu, J. Eckert, S. Pauly

J. Alloy. Compd., 708 (2017), pp. 972-981

View PDFView articleView in ScopusGoogle Scholar
[32]

Y.A. Wu, Y.H. Xiao, G.L. Chen, C.T. Liu, Z.P. Lu

Adv. Mater., 22 (2010)

2770-+

Google Scholar
[33]

X.D. Wang, R.T. Qu, Z.Q. Liu, Z.F. Zhang

Mater. Sci. Eng. A-Struct. Mater. Prop. Microstruct. Process., 696 (2017), pp. 267-272

View PDFView articleCrossrefView in ScopusGoogle Scholar
[34]

T.Y. Yan, L. Zhang, R.L. Narayan, J.Y. Pang, Y. Wu, H.M. Fu, H. Li, H.F. Zhang, U. Ramamurty

Acta Mater., 229 (2022), Article 117827

View PDFView articleView in ScopusGoogle Scholar
[35]

F. Jiang, M.Q. Jiang, H.F. Wang, Y.L. Zhao, L. He, J. Sun

Acta Mater., 59 (2011), pp. 2057-2068

View PDFView articleView in ScopusGoogle Scholar
[36]

L. Zhang, Y. Wu, S.D. Feng, W. Li, H.W. Zhang, H.M. Fu, H. Li, Z.W. Zhu, H.F. Zhang

J. Mater. Sci. Technol., 38 (2020), pp. 73-79

View PDFView articleView in ScopusGoogle Scholar
[37]

R. Raghavan, P. Murali, U. Ramamurty

Acta Mater., 57 (2009), pp. 3332-3340

View PDFView articleView in ScopusGoogle Scholar
[38]

D. Rajpoot, R.L. Narayan, L. Zhang, P. Kumar, H.F. Zhang, P. Tandaiya, U. Ramamurty

J. Mater. Sci. Technol., 106 (2022), pp. 225-235

View PDFView articleView in ScopusGoogle Scholar
[39]

J. Pan, Y.X. Wang, Q. Guo, D. Zhang, A.L. Greer, Y. Li

Nat. Commun., 9 (2018), p. 560

View in ScopusGoogle Scholar

[40]

Y. Wu, D. Cao, Y.L. Yao, G.S. Zhang, J.Y. Wang, L.Q. Liu, F.S. Li, H.Y. Fan, X.J. Liu, H. Wang, X.Z. Wang, H.H. Zhu, S.H. Jiang, P. Kontis, D. Raabe, B. Gault, Z.P. Lu

Nat. Commun., 12 (2021), p. 6582

View in ScopusGoogle Scholar
[41]

T.J. Lei, L.R. DaCosta, M. Liu, W.H. Wang, Y.H. Sun, A.L. Greer, M. Atzmon

Acta Mater., 164 (2019), pp. 165-170

View PDFView articleView in ScopusGoogle Scholar
[42]

B.S. Li, S. Xie, J.J. Kruzic

Acta Mater., 176 (2019), pp. 278-288

View PDFView articleView in ScopusGoogle Scholar
[43]

A. Gebert, A. Concustell, A.L. Greer, L. Schultz, J. Eckert

Scr. Mater., 62 (2010), pp. 635-638

View PDFView articleView in ScopusGoogle Scholar
[44]

Y.J. Huang, H.B. Fan, X.Y. Zhou, P. Xue, Z.L. Ning, D. Daisenberger, J.F. Sun, J. Shen

Scr. Mater., 103 (2015), pp. 41-44

View PDFView articleGoogle Scholar
[45]

P. Xue, S. Pauly, W.M. Gan, S.S. Jiang, H.B. Fan, Z.L. Ning, Y.J. Huang, J.F. Sun

J. Mater. Sci. Technol., 35 (2019), pp. 2221-2226

View PDFView articleView in ScopusGoogle Scholar
[46]

J. Ketkaew, R. Yamada, H. Wang, D. Kuldinow, B.S. Schroers, W. Dmowski, T. Egami, J. Schroers

Acta Mater., 184 (2020), pp. 100-108

View PDFView articleView in ScopusGoogle Scholar
[47]

W. Guo, Y.M. Shao, M. Zhao, S.L. Lu, S.S. Wu

J. Alloy. Compd., 819 (2020), Article 152997

View PDFView articleView in ScopusGoogle Scholar
[48]

W. Guo, J. Saida, M. Zhao, S.L. Lu, S.S. Wu

Mater. Sci. Eng. A-Struct. Mater. Prop. Microstruct. Process., 759 (2019), pp. 59-64

View PDFView articleView in ScopusGoogle Scholar
[49]

ASTME23-18

Standard Test Methods for Notched Bar Impact Testing of Metallic Materials

ASTM International (2018)

Google Scholar
[50]

D. Banerjee, J.C. Williams

Acta Mater., 61 (2013), pp. 844-879

View PDFView articleView in ScopusGoogle Scholar
[51]

L. Zhang, R.L. Narayan, B.A. Sun, T.Y. Yan, U. Ramamurty, J. Eckert, H.F. Zhang

Phys. Rev. Lett., 125 (2020), Article 055501

View in ScopusGoogle Scholar
[52]

L. Zhang, S. Chen, H.M. Fu, H. Li, Z.W. Zhu, H.W. Zhang, Z.K. Li, A.M. Wang, H.F. Zhang

Mater. Des., 133 (2017), pp. 82-90

View PDFView articleView in ScopusGoogle Scholar
[53]

L. Zhang, W.Q. Li, Z.W. Zhu, H.M. Fu, H. Li, Z.K. Li, H.W. Zhang, A.M. Wang, H.F. Zhang

J. Mater. Sci. Technol., 33 (2017), pp. 708-711

View PDFView articleView in ScopusGoogle Scholar
[54]

L. Zhang, H.F. Zhang, W.Q. Li, T. Gemming, Z.W. Zhu, H.M. Fu, J. Eckert, S. Pauly

Scr. Mater., 125 (2016), pp. 19-23

View PDFView articleView in ScopusGoogle Scholar
[55]

D.H. Ping, Y. Mitarai, F.X. Yin

Scr. Mater., 52 (2005), pp. 1287-1291

View PDFView articleView in ScopusGoogle Scholar
[56]

P. Tandaiya, R. Narasimhan, U. Ramamurty

Acta Mater., 61 (2013), pp. 1558-1570

View PDFView articleView in ScopusGoogle Scholar
[57]

Y.H. Sun, A. Concustell, A.L. Greer

Nat. Rev. Mater., 1 (2016), p. 16039

View in ScopusGoogle Scholar
[58]

P. Gong, G. Yin, Z. Jamili-Shirvan, H.Y. Ding, X.Y. Wang, J.S. Jin

Mater. Sci. Eng. A-Struct. Mater. Prop. Microstruct. Process., 797 (2020), Article 140078

View PDFView articleView in ScopusGoogle Scholar
[59]

Y.W. Chai, H.Y. Kim, H. Hosoda, S. Miyazaki

Acta Mater., 57 (2009), pp. 4054-4064

View PDFView articleView in ScopusGoogle Scholar
[60]

H.Y. Kim, Y. Ikehara, J.I. Kim, H. Hosoda, S. Miyazaki

Acta Mater., 54 (2006), pp. 2419-2429

View PDFView articleView in ScopusGoogle Scholar
[61]

K.K. Song, S. Wu, I. Kaban, M. Stoica, J. Bednarčík, B.A. Sun, C.D. Cao, G. Wang, L. Wang, J. Eckert

J. Alloy. Compd., 841 (2020), Article 155781

View PDFView articleView in ScopusGoogle Scholar
[62]

G. Li, Z.R. He, F. Jiang, Y.K. Wu, R. Wei, L. He, J. Sun

Mater. Sci. Eng. A-Struct. Mater. Prop. Microstruct. Process., 634 (2015), pp. 99-102

View PDFView articleView in ScopusGoogle Scholar
[63]

Y. Ren, T.Y. Yan, Z.B. Huang, Q. Zhou, K. Hua, X.L. Li, Y. Du, Q. Jia, L. Z hang, H.F. Zhang, H.F. Wang

J. Mater. Sci. Technol., 134 (2023), pp. 33-41

View PDFView articleView in ScopusGoogle Scholar
[64]

E. Bertrand, P. Castany, Y. Yang, E. Menou, T. Gloriant

Acta Mater., 105 (2016), pp. 94-103

View PDFView articleView in ScopusGoogle Scholar
[65]

X.K. Ma, Z. Chen, D.L. Zhong, S.N. Luo, L. Xiao, W.J. Lu, S.L. Zhang

J. Mater. Sci. Technol., 75 (2021), pp. 27-38

View PDFView articleView in ScopusGoogle Scholar
[66]

H.Y. Zhan, G. Wang, D. Kent, M. Dargusch

Acta Mater., 105 (2016), pp. 104-113

View PDFView articleView in ScopusGoogle Scholar
[67]

X.K. Ma, J.H. Li, Z. Chen, J.Y. Li, X.J. Zhao, F.G. Li

Mater. Sci. Eng. A-Struct. Mater. Prop. Microstruct. Process., 838 (2022), Article 142813

View PDFView articleView in ScopusGoogle Scholar
[68]

Q.Y. Zhao, Q.Y. Sun, S.W. Xin, Y.N. Chen, C. Wu, H. Wang, J.W. Xu, M.P. Wan, W.D. Zeng, Y.Q. Zhao

Mater. Sci. Eng. A-Struct. Mater. Prop. Microstruct. Process., 845 (2022), Article 143260

View PDFView articleView in ScopusGoogle Scholar
[69]

K. Yao, X.H. Min

Mater. Sci. Eng. A-Struct. Mater. Prop. Microstruct. Process., 827 (2021), Article 142044

View PDFView articleView in ScopusGoogle Scholar
[70]

I. Weiss, S.L. Semiatin

Mater. Sci. Eng. A-Struct. Mater. Prop. Microstruct. Process., 243 (1998), pp. 46-65

View PDFView articleView in ScopusGoogle Scholar
[71]

K. Wu, L.J. Zheng, H. Zhang

J. Alloy. Compd., 770 (2019), pp. 1029-1037

View PDFView articleView in ScopusGoogle Scholar
[72]

J.Q. Wang, W.H. Wang, H.Y. Bai

J. Non-Cryst. Solids, 357 (2011), pp. 220-222

View PDFView articleView in ScopusGoogle Scholar
[73]

C.C. Yuan, J.F. Xiang, X.K. Xi, W.H. Wang

Phys. Rev. Lett., 107 (2011), Article 236403

CrossrefView in ScopusGoogle Scholar
[74]

Y. Du, W.C. Han, Q. Zhou, Y.H. Xu, H.M. Zhai, V. Bhardwaj, H.F. Wang

J. Alloy. Compd., 835 (2020), Article 155247

View PDFView articleView in ScopusGoogle Scholar
[75]

J. Pan, Y.P. Ivanov, W.H. Zhou, Y. Li, A.L. Greer

Nature, 578 (2020), pp. 559-562

CrossrefView in ScopusGoogle Scholar
[76]

T.C. Hufnagel

Nat. Mater., 14 (2015), pp. 867-868

CrossrefView in ScopusGoogle Scholar
[77]

S.V. Ketov, Y.H. Sun, S. Nachum, Z. Lu, A. Checchi, A.R. Beraldin, H.Y. B ai, W.H. Wang, D.V. Louzguine-Luzgin, M.A. Carpenter, A.L. Greer

Nature, 524 (2015), p. 200

CrossrefView in ScopusGoogle Scholar
[78]

Y.H. Liu, D. Wang, K. Nakajima, W. Zhang, A. Hirata, T. Nishi, A. Inoue, M .W. Chen

Phys. Rev. Lett., 106 (2011), Article 125504

CrossrefView in ScopusGoogle Scholar
[79]

Y.H. Liu, G. Wang, R.J. Wang, D.Q. Zhao, M.X. Pan, W.H. Wang

Science, 315 (2007), pp. 1385-1388

View in ScopusGoogle Scholar
[80]

X.H. Du, J.C. Huang, K.C. Hsieh, Y.H. Lai, H.M. Chen, J.S.C. Jang, P.K. L iaw

Appl. Phys. Lett., 91 (2007), Article 131901

View in ScopusGoogle Scholar